

## RESEARCH ARTICLE

10.1002/2014JA020064

## Global morphology and spectral properties of EMIC waves derived from CRRES observations

Nigel P. Meredith<sup>1</sup>, Richard B. Horne<sup>1</sup>, Tobias Kersten<sup>1</sup>, Brian J. Fraser<sup>2</sup>, and Russell S. Grew<sup>2</sup><sup>1</sup>British Antarctic Survey, Natural Environment Research Council, Cambridge, England <sup>2</sup>Centre for Space Physics, University of Newcastle, Newcastle, New South Wales, Australia

## Key Points:

- EMIC waves are most prevalent from 12 to 18 MLT during active conditions
- Event-averaged intensity is of the order  $1 \text{ nT}^2$  during active conditions
- Results can be used to assess the role of EMIC waves on the radiation belts

## Correspondence to:

N. P. Meredith,  
nmer@bas.ac.uk

## Citation:

Meredith, N. P., R. B. Horne, T. Kersten, B. J. Fraser, and R. S. Grew (2014), Global morphology and spectral properties of EMIC waves derived from CRRES observations, *J. Geophys. Res. Space Physics*, 119, 5328–5342, doi:10.1002/2014JA020064.

Received 10 APR 2014

Accepted 7 JUN 2014

Accepted article online 11 JUN 2014

Published online 1 JUL 2014

**Abstract** Gyroresonant wave-particle interactions with electromagnetic ion cyclotron (EMIC) waves are a potentially important loss process for relativistic electrons in the Earth's radiation belts. Here we perform a statistical analysis of the EMIC waves observed by the Combined Release and Radiation Effects Satellite (CRRES) to determine the global morphology and spectral properties of the waves and to help assess their role in radiation belt dynamics. Helium band EMIC waves, with intensities,  $B_w^2$ , greater than  $0.1 \text{ nT}^2$ , are most prevalent during active conditions ( $AE > 300 \text{ nT}$ ), from  $4 < L^* < 7$  in the afternoon sector, with an average percentage occurrence of 2.7%. Hydrogen band EMIC wave events, with intensities greater than  $0.1 \text{ nT}^2$ , are also most prevalent in the afternoon sector during active conditions in the same region, but they are less frequent with an average percentage occurrence of 0.6%. The average intensity of the helium and hydrogen band EMIC waves in the region  $4 < L^* < 7$  in the afternoon sector during active conditions is  $2 \text{ nT}^2$  and  $0.5 \text{ nT}^2$ , respectively, and suggests that the waves can cause strong diffusion. However, the time-averaged properties are very different, being a factor of 30–50 lower for helium and hydrogen band EMIC waves, respectively, suggesting that the overall effect will be correspondingly weaker. Nevertheless, the moderate and strong EMIC wave events with  $B_w^2 > 0.1 \text{ nT}^2$  reported on here will contribute to relativistic electron loss in the Earth's radiation belts and should be included in radiation belt models.

## 1. Introduction

Relativistic electrons in the Earth's Van Allen radiation belts generally occupy two torus-shaped zones separated by a slot region [Van Allen and Frank, 1959]. The inner radiation belt, which extends from approximately 1.1 to 2 Earth radii ( $R_E$ ) in the geomagnetic equatorial plane, tends to remain stable except during the most intense geomagnetic storms [Baker et al., 2007]. However, the outer radiation belt, which extends from 3 to 7  $R_E$ , is highly variable [Paulikas and Blake, 1979; Baker et al., 1986]. Here the flux of relativistic electrons can change by a factor of 100 or more on a variety of timescales ranging from minutes to tens of days [e.g., Blake et al., 1992; Baker et al., 1994]. Understanding how these so-called “killer” electrons behave is important since enhanced fluxes of relativistic electrons damage satellites [Wrenn, 1995; Baker, 2001; Wrenn et al., 2002] and pose a risk to astronauts on extravehicular activities [e.g., Dachev et al., 2013].

Studies at geosynchronous orbit show that the fluxes of relativistic electrons in the outer radiation belt increase by a factor of 2 or more during approximately half of all moderate and intense storms [Reeves et al., 2003]. However, about one in five of these storms result in a reduction of the flux by a factor of 2 or more [Reeves et al., 2003]. It is thus important to study loss as well as acceleration processes. Indeed, intense relativistic electron precipitation has been observed during the recovery phase of geomagnetic storms [Clilverd et al., 2007; Millan et al., 2007; Rodger et al., 2008], and such loss will compete with any ongoing injection and/or acceleration processes. A quantitative knowledge of the loss processes is therefore essential to understand, model, and ultimately predict the dynamics of relativistic electrons in the Earth's radiation belts.

Gyroresonant wave-particle interactions play a key role in the acceleration and loss of relativistic electrons in the Earth's radiation belts [e.g., Horne, 2002; Thorne, 2010]. These interactions, which break the first and second adiabatic invariant, lead to both pitch angle and energy diffusion [e.g., Kennel and Petschek, 1966]. One potentially important interaction, whose role in radiation belt dynamics has yet to be fully evaluated, is gyroresonant pitch angle scattering by electromagnetic ion cyclotron (EMIC) waves [Horne and Thorne, 1998].

EMIC waves propagate at frequencies below the proton gyrofrequency which, in the inner magnetosphere, lie in the ultralow frequency Pc1–2 band (0.1–5 Hz). They are observed in three distinct frequency bands.

Hydrogen band EMIC waves, which are observed between the helium ion gyrofrequency,  $f_{\text{He}^+}$ , and the proton gyrofrequency,  $f_{\text{cp}}$ , are mainly found outside the plasmopause [Fraser and Nguyen, 2001]. In contrast, helium band EMIC waves, which are observed between the oxygen ion gyrofrequency,  $f_{\text{O}^+}$  and  $f_{\text{He}^+}$ , are observed both inside and outside the plasmopause [Fraser and Nguyen, 2001]. EMIC waves below  $f_{\text{O}^+}$ , referred to as oxygen band EMIC waves, are rarely observed. The excited band is controlled by the level of geomagnetic activity [Bräysy et al., 1998], the location with respect to the plasmopause [Fraser and Nguyen, 2001] and by the ion composition and anisotropy [Kozyra et al., 1984; Horne and Thorne, 1994].

EMIC waves are observed over a wide range of  $L$  shells, ranging from  $L = 3$  to  $L = 10$ . The percentage occurrence tends to increase with increasing  $L$ , irrespective of local time [e.g., Anderson et al., 1992a; Usanova et al., 2012] and maximize in the afternoon sector [Bossen et al., 1976; Roux et al., 1982; Fraser and McPherron, 1982; Clausen et al., 2011; Keika et al., 2013]. For example, using Active Magnetospheric Particle Tracer Explorers (AMPTE)/CCE data, Anderson et al. [1992a] found that EMIC waves with peak to peak amplitudes greater than 0.8 nT occurred most frequently in the region  $7 < L < 9$  for  $11 < \text{magnetic local time (MLT)} < 15$ , with a percentage occurrence of 10–20%. More recently, Usanova et al. [2012], using Time History of Events and Macroscale Interactions during Substorms (THEMIS) data together with an automated EMIC wave detection algorithm, found peak rates of the order 6–8% in the region  $8 < L < 10$  primarily in the noon and dusk sectors. In the inner magnetosphere, inside  $L = 6$ , the percentage overall occurrence is lower and typically of the order of a few percent [Erlandson and Ukhorskiy, 2001; Usanova et al., 2012]. By type, hydrogen band EMIC waves are most common in the outer magnetosphere with a percentage occurrence of the order 10% in the region  $7 < L < 9$  in the afternoon sector regardless of magnetic activity [Keika et al., 2013]. In contrast, helium band EMIC waves occur most frequently in the inner magnetosphere with a percentage occurrence of the order 5–10% in the region  $4 < L < 7$  on the prenoon to duskside under disturbed conditions ( $Dst < -50\text{nT}$ ) [Keika et al., 2013].

EMIC waves are generated by anisotropic ( $T_{\perp} > T_{\parallel}$ ) medium energy (1–100 keV) ring current ions which are formed in the inner magnetosphere during enhanced earthward convection which occurs during geomagnetic storms and substorms [Cornwall et al., 1970; Jordanova et al., 2001] and in the outer dayside magnetosphere, where they have been found to be associated with solar wind pressure fluctuations [Anderson and Hamilton, 1993; Arnoldy et al., 2005; Usanova et al., 2008]. They are preferentially excited in regions of high density and hence are strongest in regions where the ring current overlaps the plasmasphere [e.g., Yahnina et al., 2003; Pickett et al., 2010] and dayside drainage plumes [Morley et al., 2009].

EMIC waves can efficiently scatter energetic ring current ions into the loss cone and contribute to the loss of ring current ions during geomagnetic storms [Cornwall et al., 1970; Jordanova et al., 2001]. They lead to proton precipitation in the energy range 1–100 keV [e.g., Yahnina et al., 2003] and have been associated with detached subauroral proton arcs [Sakaguchi et al., 2007; Yuan et al., 2010], subauroral proton spots [Yahnina et al., 2007], and subauroral proton aurora flashes [Yahnina et al., 2008]. They are also able to resonate with highly relativistic electrons [Lyons and Thorne, 1972; Horne and Thorne, 1998; Summers et al., 1998] causing pitch angle scattering and loss to the atmosphere [Thorne, 1974; Thorne and Andreoli, 1980]. If conditions are particularly favorable, they can resonate with electrons with energies of the order of 1 MeV and may be strong enough to cause strong diffusion scattering [Meredith et al., 2003].

In a survey of over 800 EMIC wave events observed by the Combined Release and Radiation Effects Satellite (CRRES), Meredith et al. [2003] found that while the minimum resonant energy was above 2 MeV for the majority of the events, it could fall below 2 MeV for wave frequencies just below  $f_{\text{cp}}$  and  $f_{\text{He}^+}$  in regions of high plasma density and/or low magnetic field. Since the average intensity of these lower-energy scattering events ( $\sim 1 \text{ nT}^2$ ) [Meredith et al., 2003] is sufficient to cause strong diffusion scattering [Summers and Thorne, 2003], it was inferred that EMIC waves could play an important role in the loss of radiation belt electrons.

To assess the precise role of these waves in radiation belt dynamics, diffusion codes require comprehensive information on the spectral distribution of the EMIC wave magnetic field power spectral density as a function of spatial location and geomagnetic activity. Previous statistical studies have examined the occurrence of EMIC waves [e.g., Anderson et al., 1992a; Usanova et al., 2012; Keika et al., 2013] but have not examined the spectral characteristics of the waves. In this study we fit spectral profiles to the EMIC wave events observed by CRRES to obtain information on the spectral properties of the waves and to examine the distribution of the waves as a function of spatial location and magnetic activity. The instrumentation and data analysis techniques are described in section 2, followed by a description of the EMIC wave database in section 3.

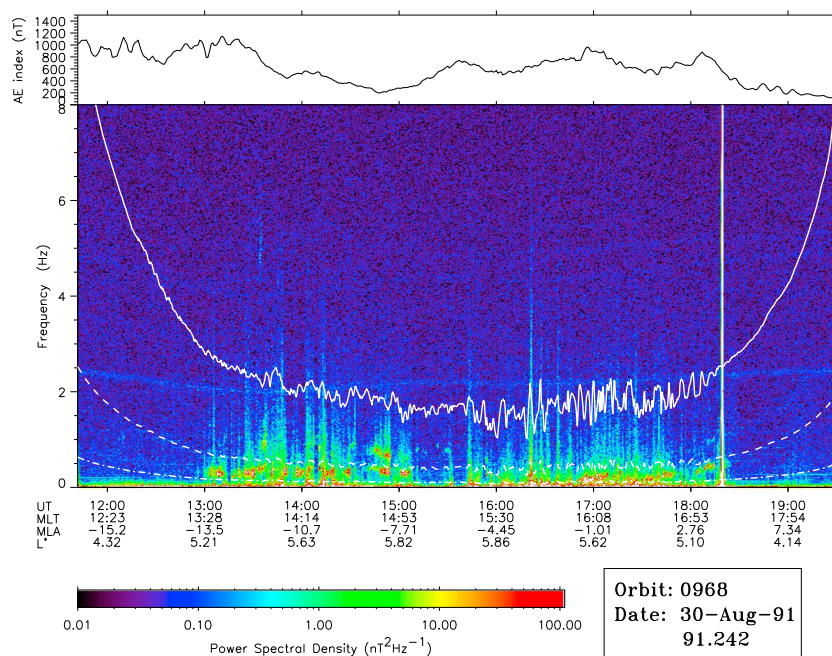


**Figure 1.** Survey plot of the wave power spectral density for CRRES (bottom) orbit 968 as a function of frequency and Universal Time, together with a trace of the (top) AE index. The solid white line denotes the proton gyrofrequency, the dashed line the helium ion gyrofrequency, and the dash-dotted line the oxygen ion gyrofrequency.

We present global maps of EMIC wave occurrence and percentage occurrence for helium and hydrogen band EMIC waves in section 4. The spectral properties of the EMIC waves are then described in section 5. Finally, the results are discussed and our conclusions are presented in sections 6 and 7, respectively.

## 2. Instrumentation and Data Analysis

CRRES was launched on 25 July 1990 into a highly elliptical ( $350 \times 35,548$  km), low-inclination ( $18.1^\circ$ ), geosynchronous transfer orbit [Johnson and Kierein, 1992]. The satellite operated in this region for approximately 15 months before finally failing on 11 October 1991. During the course of the mission the magnetic local time of apogee ranged from 08 through midnight to 14 MLT, leaving a gap in coverage near apogee primarily in the prenoon sector. The orbital period was approximately 10 h so that the satellite traversed the radiation belts about 5 times per day, giving good coverage of the radiation belt environment for approximately 15 months.

The three-component EMIC wave and main field data were provided by the fluxgate magnetometer [Singer *et al.*, 1992]. The three-component fluxgate data, sampled at 16 Hz, were analyzed orbit by orbit. The spectral analysis used a fast Fourier transform length of 1600 points with a 400 point step, corresponding to a frequency resolution of 10 mHz and a time step of 25.6 s. The resulting wave spectra covered the frequency range from 0 to 8 Hz in steps of 10 mHz at a time resolution of 25.6 s. A typical wave survey spectrogram from the fluxgate magnetometer during the CRRES mission is shown in Figure 1. Here the wave power spectral density in  $\text{nT}^2\text{Hz}^{-1}$  is plotted as a function of frequency and Universal Time (UT) for orbit 968 (Figure 1, bottom), together with a trace of the AE index (Figure 1, top). The Universal Time is marked at hourly intervals together with the magnetic local time, MLT, the magnetic latitude,  $\lambda_m$ , and  $L^*$  [Roederer, 1970]. The solid white line denotes the proton gyrofrequency, the dashed line the helium ion gyrofrequency, and the dash-dotted line the oxygen ion gyrofrequency. During this orbit strong helium band EMIC waves are seen between 13:00 and 15:10 UT and between 17:00 and 18:20 UT. These observations were made during high geomagnetic activity in the afternoon sector over a range of  $L^*$  (5.1–5.8). Some strong hydrogen band EMIC waves were also observed just before 15:00 UT, but they only lasted for about 10 min and were not as extensive as the helium band waves.

The period of enhanced EMIC waves during the outbound leg is shown in more detail in Figure 2. Here the wave power spectral density is plotted as a function of frequency and UT from 0 to 2 Hz and 12:30

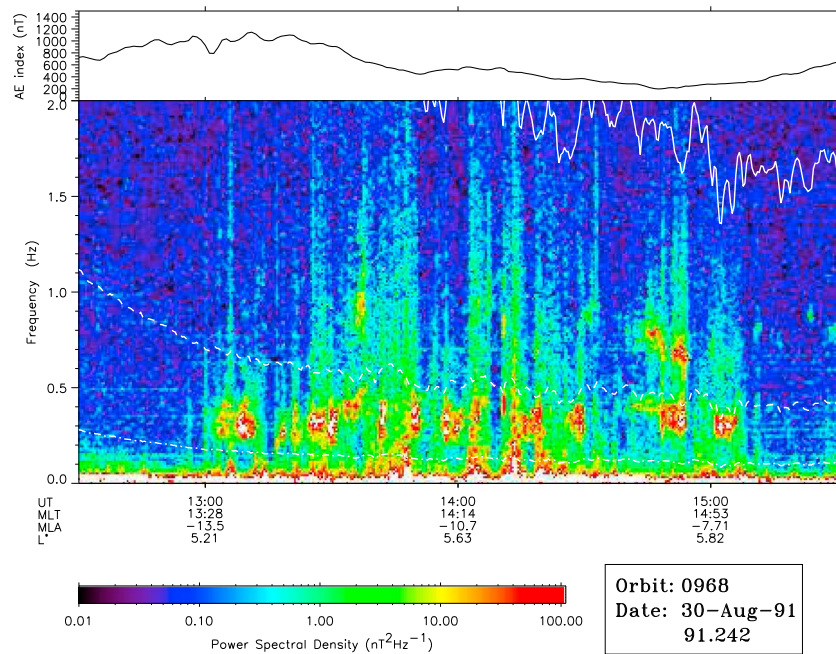


**Figure 2.** Expanded plot of the wave power spectral density from 12:30 to 15:30 UT on 30 August 1991 during CRRES orbit 968 as a function of frequency and Universal Time, together with a trace of the (top) AE index in the same format as Figure 1.

to 15:30 UT, respectively. The bursty nature of the waves is apparent with strong waves appearing and disappearing on a timescale of minutes.

For our chorus wave database [Meredith *et al.*, 2012] we initially averaged the wave data as a function of  $L^*$  and half orbit in steps of  $0.1L^*$ . The dwell time in each  $0.1L^*$  bin ranged from several minutes to tens of minutes depending on location. Since the EMIC waves may come and go on a timescale of minutes averaging the data into bins of length  $0.1L^*$  would result in the loss of key information on the power and its spectral distribution. The best way to preserve the spectral information is to analyze each individual spectral profile and here we fit each individual spectral profile with two Gaussian functions, one in the helium band and the other in the hydrogen band. This approach has the advantage of removing noise spikes and bands which do not have Gaussian profiles. The statistics can then be conducted on the resulting fit parameters. We, therefore, fitted a Gaussian profile to the wave power spectral density, PSD, in each band of the form

$$PSD = PSD_m e^{-\left(\frac{f-f_m}{df}\right)^2} \tag{1}$$

where  $PSD_m$  is the peak power spectral density,  $f_m$  is the peak frequency, and  $df$  is the width. Since helium band EMIC waves can be observed close to the helium ion gyrofrequency, as observed in this example, for these waves we fit to the data between the oxygen ion gyrofrequency and 0.05 Hz above the helium ion gyrofrequency to make sure that we capture all of the appropriate power. Hydrogen band EMIC waves tend to be observed at frequencies well below the proton gyrofrequency and for these waves we fit to the data between the helium ion gyrofrequency and the proton gyrofrequency.

The wave power spectral density at 15:01 UT on 30 August 1991 is plotted as a function of frequency in Figure 3. The linear least squares best fit to a Gaussian profile is shown in green and the local helium ion gyrofrequency is shown as a dotted red vertical line. The peak frequency is 0.312 Hz, the spectral width is 0.053 Hz, and the intensity is 2.6  $nT^2$ . This is an example of a strong wave ( $B_w^2 > 1 nT^2$ ) observed in a region where the ratio of the electron plasma frequency,  $f_{pe}$  to the electron gyrofrequency,  $f_{ce}$  is high ( $f_{pe}/f_{ce} > 10$ ) with a peak frequency  $> 0.6f_{CHe+}$ . This type of event could play a significant role in radiation belt loss [Meredith *et al.*, 2003]. The question is how often does this type of event occur and what fraction of the events result in the strong diffusion of electrons with energies of the order 1 MeV.

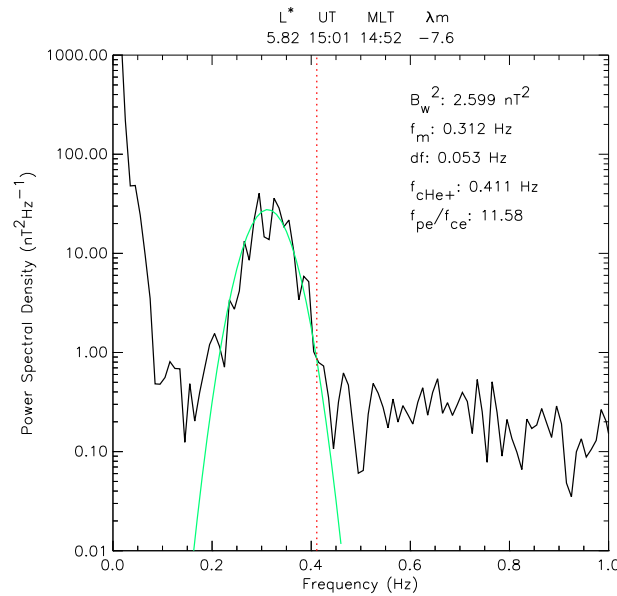


**Figure 3.** Trace of the wave spectral density as a function of frequency at 15:01 UT on 30 August 1991. The Gaussian fit is shown in green. The dotted red line represents the helium ion gyrofrequency.

A summary of the results for orbit 968 are presented in Figure 4. Figure 4 (top row) shows the wave intensity (left), the peak frequency (middle), and the spectral width (right) as a function of UT for the helium band (blue) and the hydrogen band (red) EMIC waves. Figure 4 (middle row) shows the ratio  $f_{pe}/f_{ce}$  (left), the peak frequency of the helium, and hydrogen band waves normalized to the local helium and local proton gyrofrequency respectively (middle), and the peak frequency of the helium and hydrogen band waves normalized to the equatorial helium and proton gyrofrequency respectively (right) as a function of UT. Figure 4 (bottom row) shows the spacecraft location as a function of  $L^*$  (left), MLT (middle), and  $\lambda_m$  (right) as a function of UT.

During this orbit bursty helium band EMIC waves were observed for a large portion

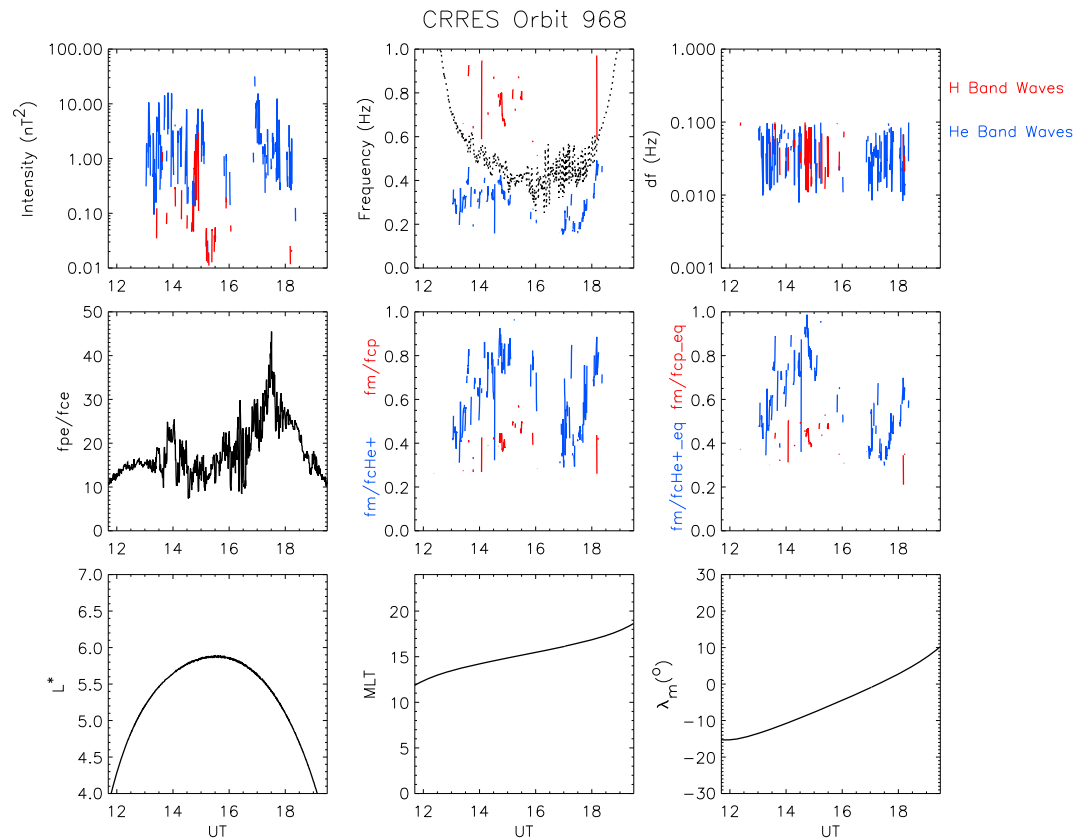


**Figure 4.** Summary plot of the results of the EMIC wave fitting for orbit 968. (top row, from left to right) Wave intensity, peak frequency, and spectral width as a function of UT for the helium band (blue) and the hydrogen band (red) EMIC waves. (middle row, from left to right) Ratio  $f_{pe}/f_{ce}$ , peak frequency of the helium and hydrogen band waves normalized to the local helium and local proton gyrofrequency, respectively, and peak frequency of the helium and hydrogen band waves normalized to the equatorial helium and proton gyrofrequency, respectively, as a function of UT. (bottom row, from left to right)  $L^*$ , MLT, and  $\lambda_m$  as a function of UT.

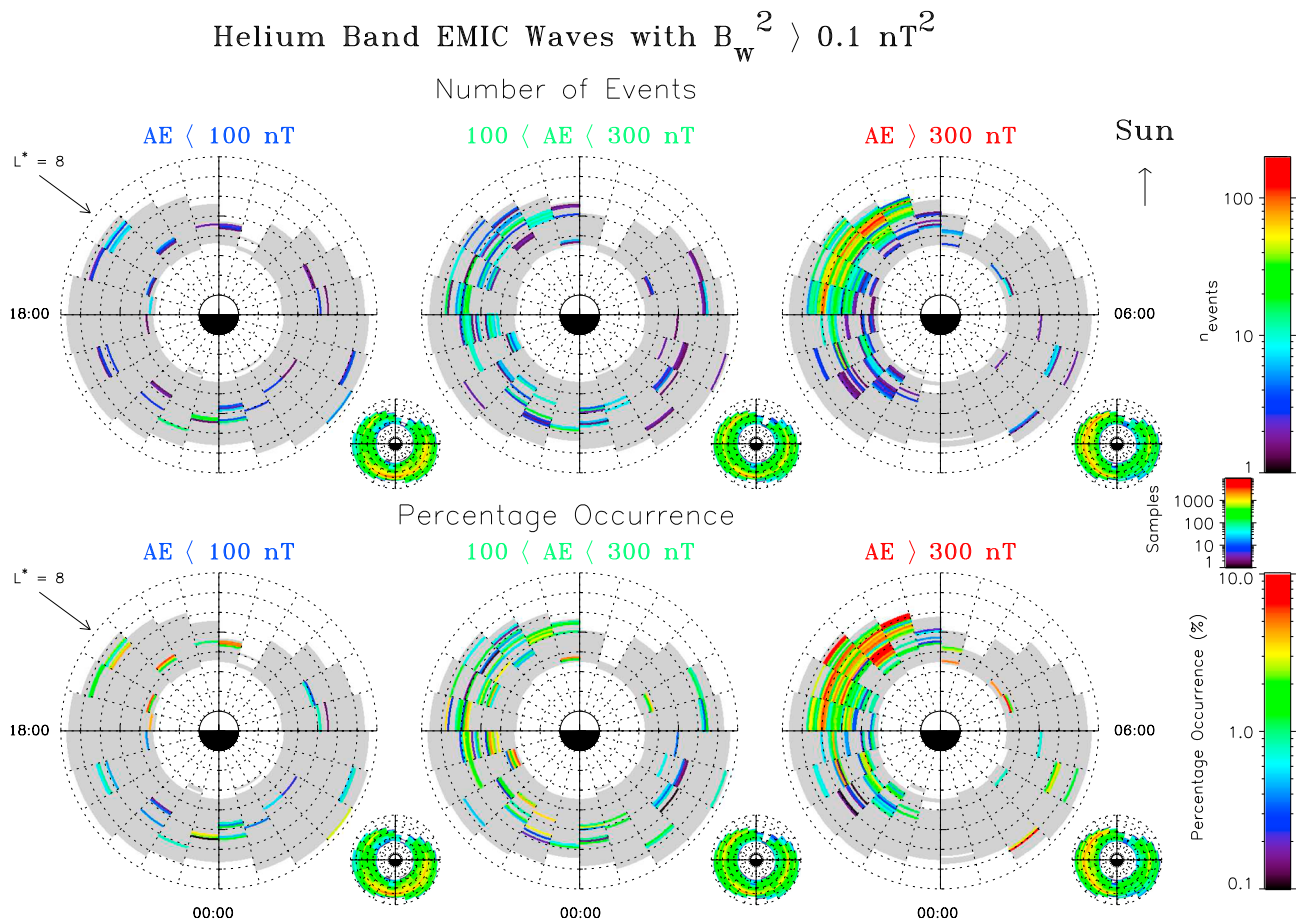


**Figure 5.** (top) Number of helium band EMIC wave events greater than  $0.1 \text{ nT}^2$  as a function of  $L^*$  and MLT for, from left to right, quiet, moderate, and active conditions. The number of events is shown in the large panels and the corresponding number of samples is shown in the small panels. In the large panels regions that were covered by CRRES but contain no EMIC wave events are shaded grey. Regions at low  $L^*$  ( $L^* < \sim 3.2$ ), where EMIC waves cannot be identified in the data, and regions at high  $L^*$  not sampled by CRRES are color-coded white. (bottom) Percentage occurrence of helium band EMIC wave events greater than  $0.1 \text{ nT}^2$  in the same format.

of the interval from 13:00 to 18:20 UT. During this period the spacecraft was located in the afternoon sector in the region  $5.1 < L^* < 5.9$  over a range of magnetic latitudes from  $-15^\circ$  to the magnetic equator. The intensities of the observed helium band waves ranged from  $0.1$  to  $10 \text{ nT}^2$  and peak frequencies covered a range of normalized frequencies from  $0.3$  to  $0.9f_{\text{cHe}^+}$ . There are a number of interesting helium band EMIC wave events during this orbit with  $f_m > 0.6f_{\text{cHe}^+}$  and intensities greater than  $1 \text{ nT}^2$  in regions of  $f_{\text{pe}}/f_{\text{ce}} > 10$  which could result in significant diffusion rates for  $1 \text{ MeV}$  electrons. The hydrogen band EMIC waves were largely observed between 1300 and 1600 UT and were less intense with normalized frequencies between  $0.3$  and  $0.5f_{\text{cp}}$ .

### 3. EMIC Wave Database

In the inner magnetosphere observations from CRRES suggest that EMIC waves are excited over a broad latitudinal range within  $\pm 11^\circ$  of the magnetic equator [Loto'aniu *et al.*, 2005]. While the CRRES orbital coverage extends to  $\pm 30^\circ$  magnetic latitude, the majority of the EMIC wave events are restricted to within  $\pm 20^\circ$  of the magnetic equator [Meredith *et al.*, 2003]. Given the broad source region, the limited latitudinal extent of the majority of the wave events observed by CRRES, and uncertainties in the external magnetic field, particularly during active conditions [McCollough *et al.*, 2008], we conduct our analysis by normalizing the observed frequency to the local proton gyrofrequency.

The three-component fluxgate data, sampled at  $16 \text{ Hz}$ , were analyzed orbit by orbit. In a previous study of CRRES EMIC wave data Fraser and Nguyen [2001] identified 830 EMIC wave event intervals, from 169 of their

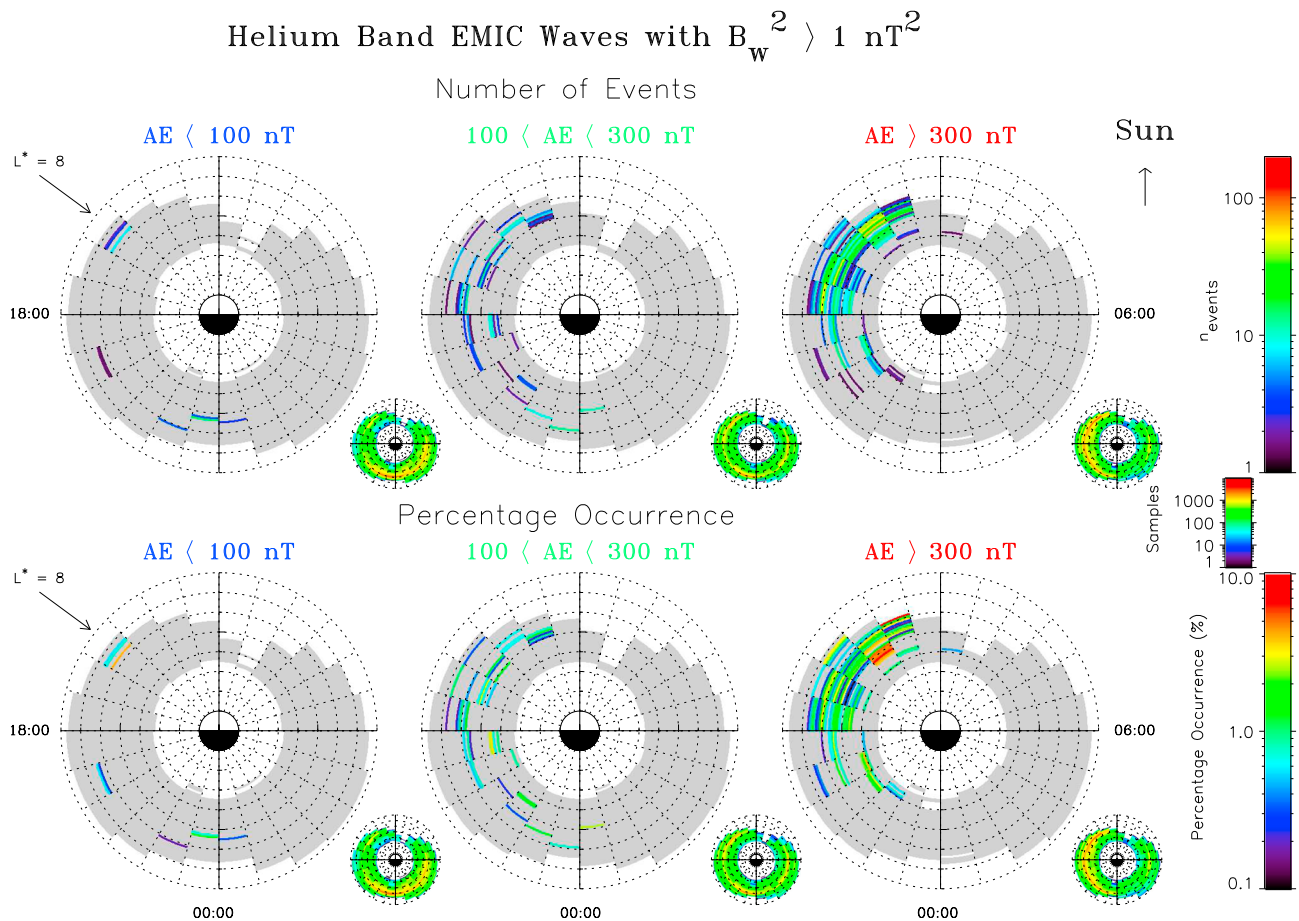


**Figure 6.** (top) Number of helium band EMIC wave events greater than  $1 \text{ nT}^2$  and (bottom) percentage occurrence of helium band EMIC wave events with intensities greater than  $1 \text{ nT}^2$  in the same format as Figure 5.

analyzed 906 orbits, covering 96 h of the analyzed 7248 h, equivalent to 1.33% of the total observations. For each event interval we performed Gaussian fits to the wave data in the hydrogen and helium band at the 25.6 s resolution of the data set. For each successful fit we recorded the band, the peak spectral density, the peak frequency, the spectral width, and the wave intensity integrated over the wave band. We then constructed two databases, one for the helium and one for the hydrogen band waves. In each database we recorded the Universal Time, the satellite position in magnetic coordinates ( $L^*$ , MLT,  $\lambda_m$ ), the geomagnetic activity as monitored by the *AE*, *Dst*, and *Kp* indices, the local proton gyrofrequency, and the plasma frequency. This information was stored for each wave spectra in each of the 906 orbits. When a successful fit was achieved, we also stored the fit parameters as described above. For the database  $L^*$  and MLT were computed using the Office National d'Etudes et de Recherche Aérospatiales Département Environnement Spatial (ONERA-DESP) library V4.2, (*D. Boscher et al.*, ONERA DESP library V4.2, 2008) with the International Geomagnetic Reference Field at the middle of the appropriate year and the Olson-Pfitzer quiet time model [*Olson and Pfitzer*, 1977]. Since the ONERA DESP library is designed for particles and we are using it for waves, we calculate  $L^*$  assuming a local pitch angle of  $90^\circ$ . The magnetic latitude was calculated using a simple dipole magnetic latitude, and the local proton gyrofrequency was calculated from the local ambient magnetic field determined by the fluxgate magnetometer instrument [*Singer et al.*, 1992]. The plasma density was derived from measurements of the plasma wave spectra by the Plasma Wave Experiment [*Anderson et al.*, 1992b] as described in *Meredith et al.* [2002].

#### 4. Global Morphology

Since the occurrence rate of EMIC waves in the inner magnetosphere is associated with disturbed conditions [e.g., *Usanova et al.*, 2012; *Keika et al.*, 2013], we conducted a statistical analysis of the wave

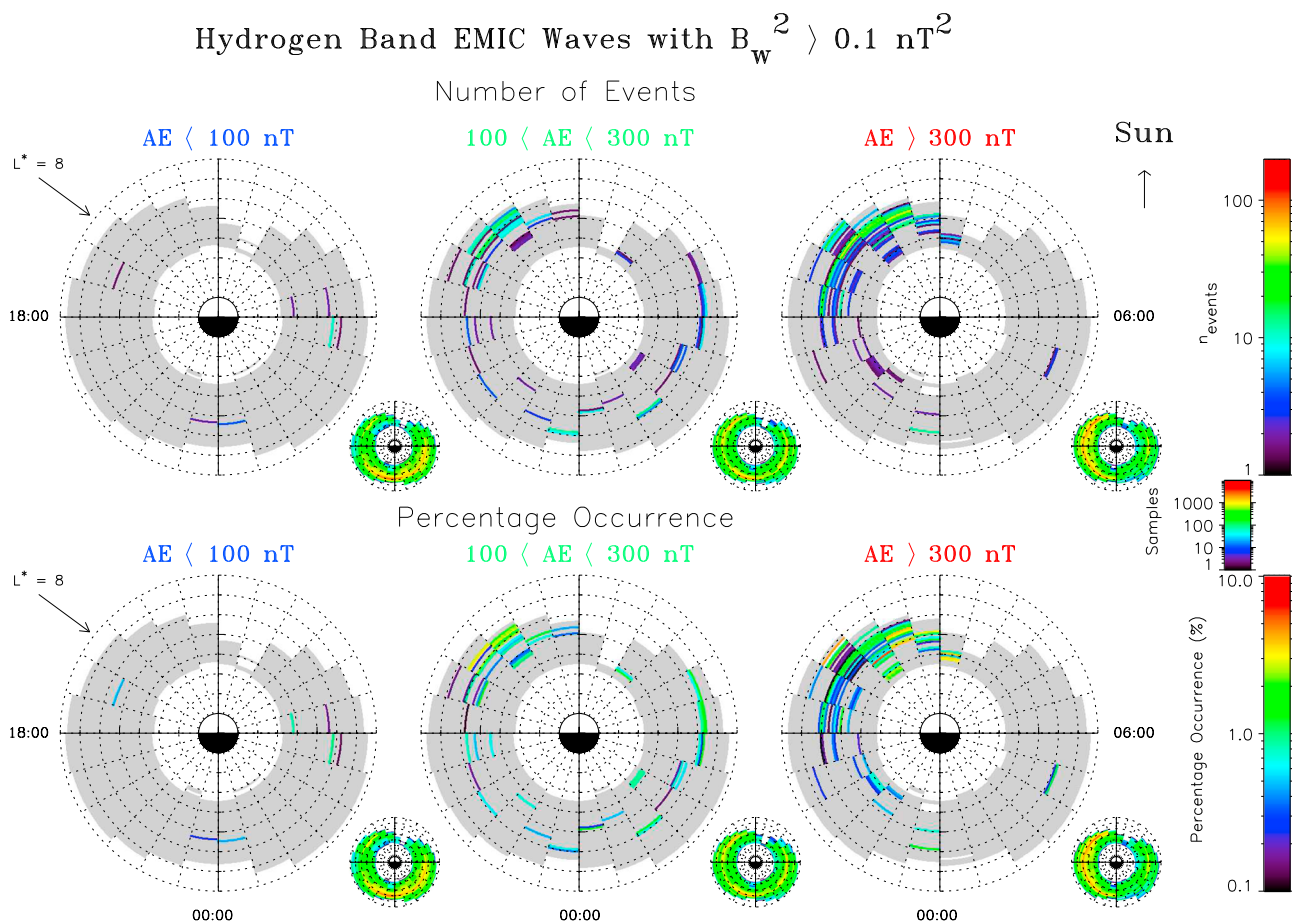


**Figure 7.** (top) Number of hydrogen band EMIC wave events greater than  $0.1 \text{ nT}^2$  and (bottom) percentage occurrence of hydrogen band EMIC wave events greater than  $0.1 \text{ nT}^2$  in the same format as Figure 5.

databases to obtain global maps of the number of events and percentage occurrence for waves above given thresholds in each of the bands as a function of geomagnetic activity as monitored by the AE index. The geomagnetic activity was divided into three levels according to the value of the AE index at the time of the measurement, which we defined to be quiet when  $AE < 100 \text{ nT}$ , moderate when  $100 < AE < 300 \text{ nT}$  and active when  $AE > 300 \text{ nT}$ . The resulting global maps for the helium band and hydrogen band waves are presented in sections 4.1 and 4.2, respectively.

#### 4.1. Helium Band EMIC Waves

The number of helium band EMIC wave events for which  $B_w^2 > 0.1 \text{ nT}^2$  is plotted as a function of  $L^*$ , MLT, and geomagnetic activity in Figure 5 (top), for, from left to right, quiet, moderate, and active conditions. The number of events is shown in the large panels and the corresponding number of samples is shown in the small panels. In the large panels regions that were covered by CRRES but contain no EMIC wave events are shaded grey. Regions at low  $L^*$  ( $L^* < \sim 3.2$ ), where EMIC waves cannot be identified in the data due to the high background magnetic field, and regions at high  $L^*$  not sampled by CRRES are color-coded white. Each plot extends linearly out to  $L^* = 8$  with noon at the top and dawn to the right. The percentage occurrence of helium band EMIC waves with  $B_w^2 > 0.1 \text{ nT}^2$  is plotted as a function of  $L^*$ , MLT, and geomagnetic activity in Figure 5 (bottom) in the same format. Helium band EMIC waves are rare during quiet conditions with intensities exceeding  $0.1 \text{ nT}^2$  for only 0.06% of the time in the region  $4 < L^* < 7$  over all MLT. They are observed more frequently during moderate conditions with intensities greater than  $0.1 \text{ nT}^2$  in the region  $4 < L^* < 7$  over all MLT for 0.3% of the time. Helium band EMIC waves are most prevalent during active conditions, with intensities greater than  $0.1 \text{ nT}^2$  being observed 1.2% of the time in the region  $4 < L^* < 7$  over all MLT. By sector the largest percentage occurrence is in the noon to dusk sector during active conditions, where intensities exceed  $0.1 \text{ nT}^2$  2.7% of the time.

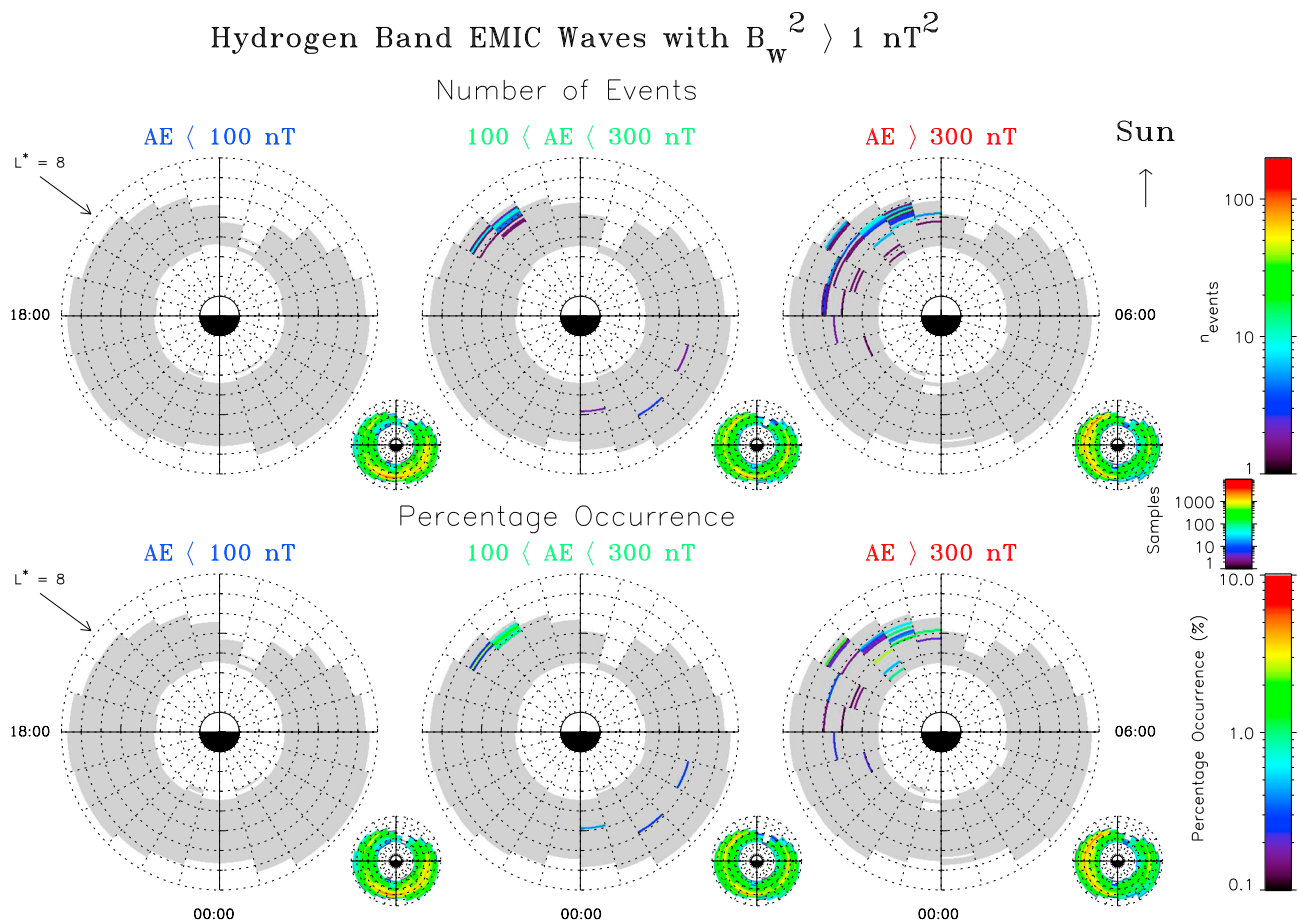


**Figure 8.** (top) Number of hydrogen band EMIC wave events greater than  $1 \text{ nT}^2$  and (bottom) percentage occurrence of hydrogen band EMIC wave events greater than  $1 \text{ nT}^2$  in the same format as Figure 5.

EMIC waves with intensities greater than  $1 \text{ nT}^2$  are typically required to put resonant electrons on strong diffusion [Thorne and Kennel, 1971; Summers and Thorne, 2003]. The number of helium band EMIC wave events for which  $B_w^2 > 1 \text{ nT}^2$  is plotted as a function of  $L^*$ , MLT and geomagnetic activity in Figure 6, together with the corresponding percentage occurrence. Helium band EMIC waves with intensities greater than  $1 \text{ nT}^2$  are rarely seen during quiet and moderate conditions. Helium band EMIC waves with intensities greater than  $1 \text{ nT}^2$  are most prevalent during active periods, being observed 0.5% of the time in the region  $4 < L^* < 7$  over all MLT. By sector the largest percentage occurrence is again in the noon to dusk sector during active conditions where waves with intensities greater than  $1 \text{ nT}^2$  are seen approximately 1% of the time.

#### 4.2. Hydrogen Band EMIC Waves

The number of hydrogen band EMIC wave events for which  $B_w^2 > 0.1 \text{ nT}^2$  is plotted as a function of  $L^*$ , MLT and geomagnetic activity in Figure 7, together with the corresponding percentage occurrence. Hydrogen band EMIC waves are very rare during quiet conditions with intensities exceeding  $0.1 \text{ nT}^2$  for only 0.008% of the time in the region  $4 < L^* < 7$  over all MLT. They are also rare during moderate conditions with intensities greater than  $0.1 \text{ nT}^2$  in the region  $4 < L^* < 7$  over all MLT for 0.1% of the time. Hydrogen band EMIC waves are most prevalent during active conditions, with intensities greater than  $0.1 \text{ nT}^2$  being observed for 0.26% of the time in the region  $4 < L^* < 7$  over all MLT. By sector the largest percentage occurrence is in the noon to dusk sector during active conditions where waves with intensities greater than  $0.1 \text{ nT}^2$  are seen 0.6% of the time.

The number of hydrogen band EMIC wave events for which  $B_w^2 > 1 \text{ nT}^2$  is plotted as a function of  $L^*$ , MLT, and geomagnetic activity in Figure 8, together with the corresponding percentage occurrence. Hydrogen band EMIC waves with intensities greater than  $1 \text{ nT}^2$  are never seen during quiet conditions and are very rare during moderate conditions. Hydrogen band EMIC waves with intensities greater than  $1 \text{ nT}^2$  are also rare

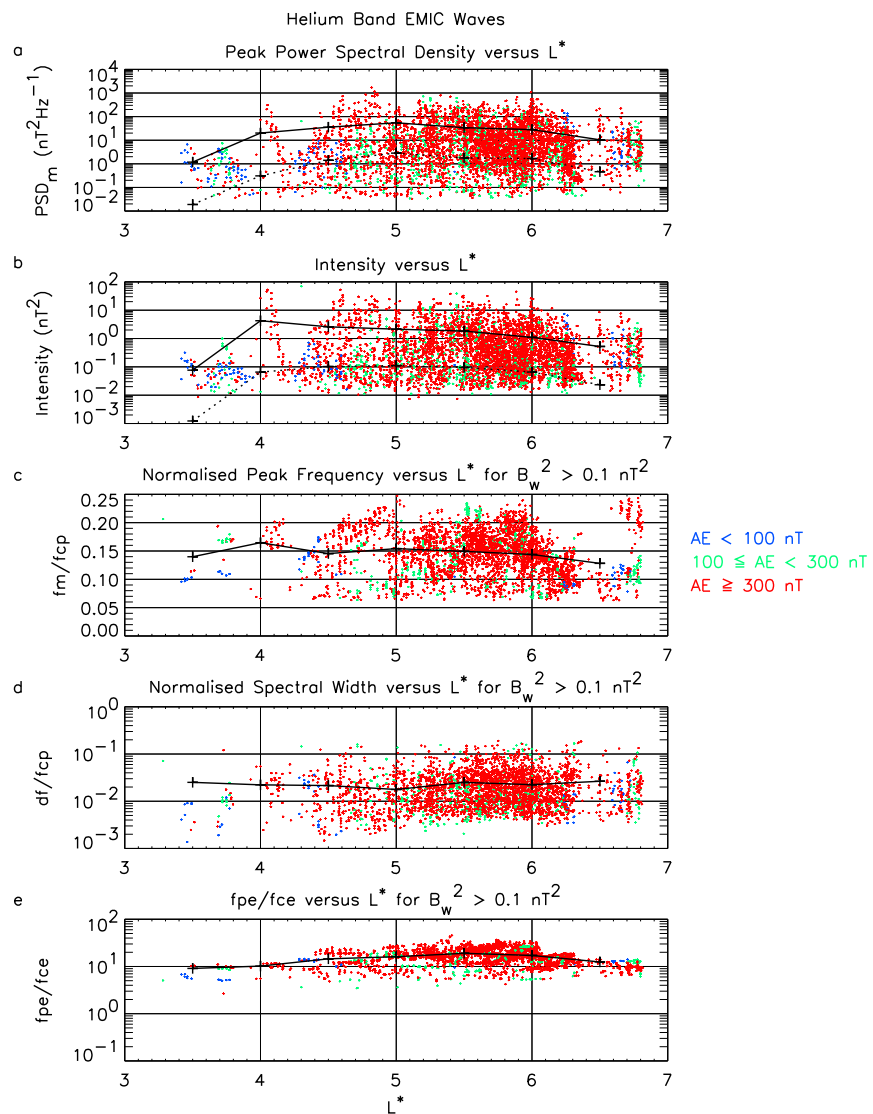


**Figure 9.** Scatter plot of the spectral properties of the helium band EMIC waves and the ratio  $f_{pe}/f_{ce}$  as a function of  $L^*$  in the afternoon sector. (a) The power spectral density, (b) the intensity, (c) the normalized peak position, (d) the spectral width, and (e) the ratio  $f_{pe}/f_{ce}$ , color-coded according to the geomagnetic activity as monitored by the AE index.

during active periods being observed 0.04% of the time in the region  $4 < L^* < 7$  over all MLT. By sector the largest percentage occurrence is again in the noon to dusk sector during active conditions but waves with intensities greater than  $1 \text{ nT}^2$  are only seen 0.09% of the time in this region.

### 5. Spectral Properties

Information on the spectral properties of the helium and hydrogen band EMIC waves is required to assess the role of the waves in radiation belt dynamics. Figure 9 shows a scatter plot of the wave parameters for the helium band EMIC wave events as a function of  $L^*$  in the afternoon sector, where the majority of the helium band EMIC wave events occur. The peak power spectral density and the intensity are shown as a function of  $L^*$  in Figures 9a and 9b, respectively. In these panels the solid and dotted lines represent the event-averaged and time-averaged value of the plotted parameter, respectively, for active conditions. The normalized peak frequency, normalized spectral width, and the ratio  $f_{pe}/f_{ce}$  are shown as a function of  $L^*$  for the more significant EMIC wave events, with  $B_w^2 > 0.1 \text{ nT}^2$ , in Figures 9c to 9e, respectively. In these panels the solid lines represent the corresponding event-averaged values for active conditions. The intensity (Figure 9b) covers over 3 orders of magnitude, ranging from 0.01 to greater than  $10 \text{ nT}^2$ . The average value of a helium band

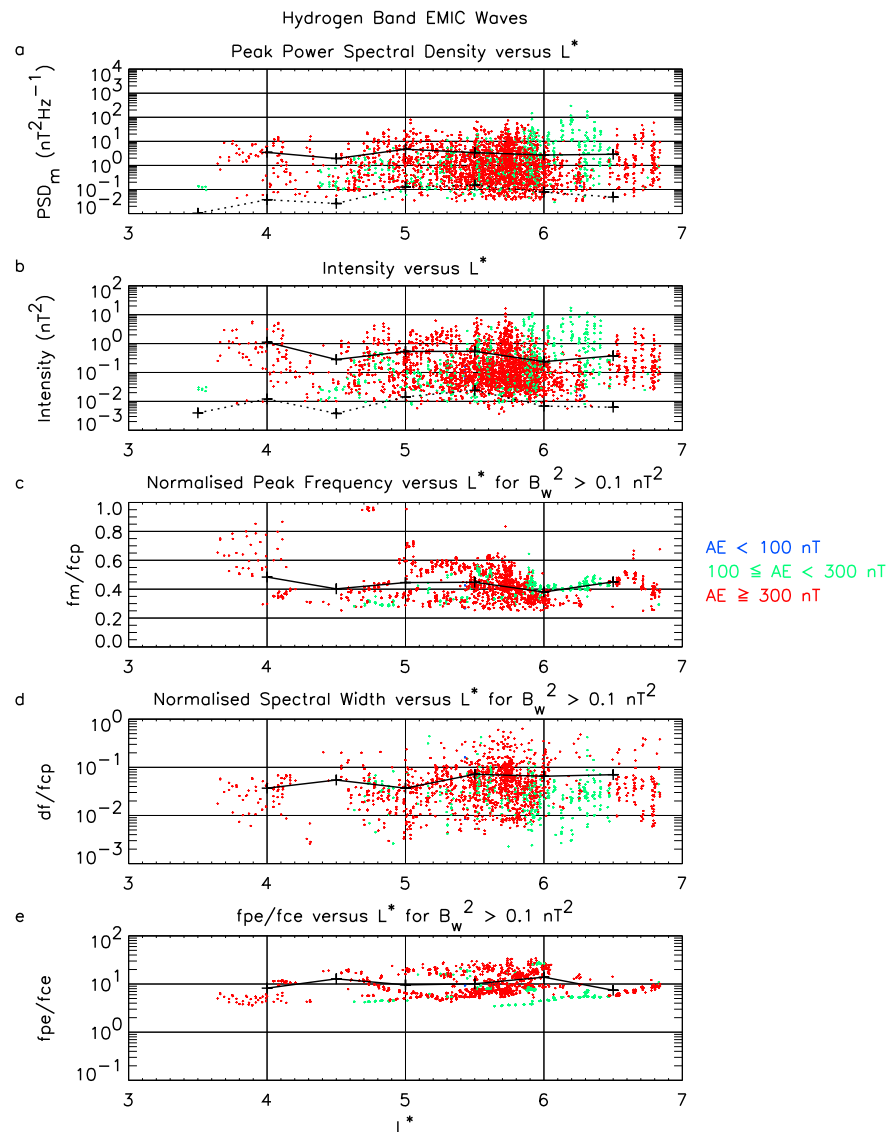


**Figure 10.** Scatter plot of the spectral properties of the hydrogen band EMIC waves and the ratio  $f_{pe}/f_{ce}$  as a function of  $L^*$  in the afternoon sector. (a) The power spectral density, (b) the intensity, (c) the normalized peak position, (d) the spectral width, and (e) the ratio  $f_{pe}/f_{ce}$ , color-coded according to the geomagnetic activity as monitored by the AE index.

EMIC wave event during active conditions is of the order of  $2 \text{ nT}^2$  (solid line). However, when all observations are taken into account, the time-averaged helium band EMIC wave intensity is much lower, typically  $0.07 \text{ nT}^2$  (dashed line). The peak frequency for the helium band wave events with  $B_w^2 > 0.1 \text{ nT}^2$  (Figure 9c) ranges from just above the oxygen ion gyrofrequency to just below the helium ion gyrofrequency. However, the bulk of the events lie between  $0.1$  and  $0.2f_{cp}$  with an average value of  $0.15f_{cp}$  which shows no significant variation with  $L^*$ . The spectral widths of the helium band wave events with  $B_w^2 > 0.1 \text{ nT}^2$  (Figure 9d) vary by an order of magnitude with an average value of  $0.02f_{cp}$  during active conditions. The ratio of  $f_{pe}/f_{ce}$  (Figure 9e) is an important parameter that determines the resonant energy, and hence, the energy where electron diffusion is likely to be most effective. The ratio  $f_{pe}/f_{ce}$  during the helium band EMIC wave events with  $B_w^2 > 0.1 \text{ nT}^2$  (Figure 9e) is large and typically greater than 10.

Figure 10 shows a scatter plot of the wave parameters for the hydrogen band EMIC wave events as a function of  $L^*$  in the afternoon sector in the same format as for Figure 9. The intensity (Figure 10b) covers 3 orders of magnitude, ranging from 0.01 to greater than  $10 \text{ nT}^2$ . The average value of a hydrogen band EMIC wave event during active conditions is of the order of  $0.5 \text{ nT}^2$  (solid line). However, when all observations are

taken into account, the time-averaged hydrogen band EMIC wave intensity is much lower, typically less than  $0.01 \text{ nT}^2$  (dashed line). The peak frequency for the hydrogen band wave events with more significant wave power ranges (Figure 10c) from just above the helium ion gyrofrequency to about  $0.6f_{\text{cp}}$ , with an average value of  $0.4f_{\text{cp}}$  which shows no significant variation with  $L^*$ . The spectral widths of the hydrogen band wave events with  $B_w^2 > 0.1 \text{ nT}^2$  (Figure 10d) vary by more than an order of magnitude with an average value of  $0.05f_{\text{cp}}$  during active conditions. The ratio  $f_{\text{pe}}/f_{\text{ce}}$  during the hydrogen band EMIC wave events with  $B_w^2 > 0.1 \text{ nT}^2$  (Figure 10e) is also large and typically around 10.

## 6. Discussion

Our observations show that both hydrogen band and helium band EMIC waves are substorm dependent and occur most frequently in the region  $4 < L^* < 7$  in the postnoon sector during active conditions. The EMIC wave percentage occurrences reported here are generally consistent with the results from the AMPTE CCE [Anderson *et al.*, 1992a], CRRES [Fraser and Nguyen, 2001], and THEMIS [Usanova *et al.*, 2012] in this region. The location of the observed waves and their dependence on magnetic activity suggest that the waves observed by the CRRES satellite are most likely generated by anisotropic ring current ions injected into this region during enhanced convection associated with the enhanced magnetic activity. We note that larger percentage occurrences are observed further out ( $L^* > 7$ ) on the dayside [e.g., Anderson *et al.*, 1992b; Usanova *et al.*, 2012] in association with magnetospheric compressions, but this region was not sampled by the CRRES missions and is not studied here. A second, albeit smaller, peak in EMIC wave occurrence has also been observed near dawn [e.g., Anderson *et al.*, 1992a], but this peak occurs further out at  $L > 8$ , in a region not sampled by the CRRES satellite.

In the inner magnetosphere EMIC waves are generated by anisotropic medium energy ring current ions injected during storms and substorms [Cornwall *et al.*, 1970; Jordanova *et al.*, 2001] so that a measure of the ring current, such as the *Dst* index might also be expected to be a useful proxy for EMIC waves. To investigate this possibility, we repeated the analysis using the *Dst* index to monitor the geomagnetic activity but found no obvious trend with decreasing *Dst*. This is most likely due to the fact that substorm activity, and hence EMIC wave generation, can be prolonged and enhanced during high-speed solar wind streams, which have little or no significant signatures in *Dst* [e.g., Denton and Borovsky, 2008] and also during the recovery phase of geomagnetic storms when the *Dst* index is returning to quiet time levels.

The average intensity of the helium and hydrogen band EMIC waves in the region  $4 < L^* < 7$  in the afternoon sector during active conditions is  $2 \text{ nT}^2$  and  $0.5 \text{ nT}^2$ , respectively, and suggests that the waves can cause strong diffusion [e.g., Summers and Thorne, 2003]. However, the time-averaged properties are very different, being a factor of 30–50 lower for helium and hydrogen band EMIC waves, respectively, suggesting that the overall effect will be correspondingly much weaker. This raises a conceptually difficult question: do several short duration bursts of EMIC waves that could cause strong diffusion locally give the same results as averaging the wave intensity and applying the lower average diffusion rates over the drift path of the electrons? This is beyond the scope of this study but it is one that may be addressed by radiation belt codes.

Previous studies have shown that helium band minimum resonant energies fall below 2 MeV in regions of high plasma density and/or low magnetic field ( $f_{\text{pe}}/f_{\text{ce}} > 10$ ) and are associated with wave frequencies in the range  $0.6f_{\text{che}^+} < f < f_{\text{che}^+}$  [Meredith *et al.*, 2003]. Of the 1286 helium band EMIC wave events with intensities greater than  $1 \text{ nT}^2$  during active conditions in the region 12–18 MLT, 574 have peak frequencies in the range  $0.6f_{\text{che}^+} < f < f_{\text{che}^+}$  and are observed in regions of  $f_{\text{pe}}/f_{\text{ce}} > 10$ . This equates to approximately 0.5% of the observations during active conditions in this region, suggesting that helium band EMIC waves can drive strong diffusion of electrons with energies in the range  $1 < E < 2 \text{ MeV}$ , but that it is relatively rare.

Hydrogen band minimum resonant energies fall below 2 MeV in regions of high plasma density and/or low magnetic field ( $f_{\text{pe}}/f_{\text{ce}} > 10$ ) and are associated with wave frequencies in the range  $0.4f_{\text{cp}} < f < f_{\text{cp}}$  [Meredith *et al.*, 2003]. Of the 102 helium band EMIC wave events with intensities greater than  $1 \text{ nT}^2$  during active conditions in the region 12–18 MLT, 13 have peak frequencies in the range  $0.4f_{\text{cp}} < f < f_{\text{cp}}$  and are observed in regions of  $f_{\text{pe}}/f_{\text{ce}} > 10$ . This equates to approximately 0.01% of the observations during active conditions in this region and suggests that hydrogen band EMIC waves do not contribute to the strong diffusion of  $< 2 \text{ MeV}$  electrons.

Our results suggest that EMIC waves will contribute to relativistic electron loss during enhanced geomagnetic activity. The wave properties determined in this study can be used to calculate energy and pitch angle diffusion coefficients [Glauert and Horne, 2005] for use in radiation belt models [e.g., Glauert et al., 2014], to assess the role of EMIC waves in radiation belt dynamics. Indeed, there is evidence linking EMIC waves to relativistic electron precipitation [Millan et al., 2007; Miyoshi et al., 2008; Carson et al., 2013], but it is unlikely to be strong enough or persistent enough to give rise to the electron flux dropouts commonly seen during the storm main phase, as established by recent particle observations [Horne et al., 2009; Meredith et al., 2011; Turner et al., 2012].

## 7. Conclusions

We have used CRRES data to develop a global model of the percentage occurrence of hydrogen and helium band EMIC waves and to examine the spectral properties of the waves. Our principle findings are the following:

1. Helium band EMIC waves, with intensities greater than  $0.1 \text{ nT}^2$ , are most prevalent during active conditions from  $4 < L^* < 7$  in the afternoon sector, with an average percentage occurrence of 2.7%.
2. Hydrogen band EMIC wave events, with intensities greater than  $0.1 \text{ nT}^2$ , are also most prevalent in the noon to dusk sector during active conditions in the same region, but they are less frequent than the corresponding helium band wave events with an average percentage occurrence of 0.6%.
3. The average intensity of a helium band wave event during active conditions in the afternoon sector, where the waves are most frequent, is of the order  $2 \text{ nT}^2$ . However, the time-averaged intensity of the helium band EMIC waves during active conditions in this region is about a factor of 30 lower.
4. The average peak frequency and width of the moderate and strong helium band wave events ( $B_w^2 > 0.1 \text{ nT}^2$ ) during active conditions, in the afternoon sector where the waves are most frequent, is  $0.15f_{cp}$  and  $0.02f_{cp}$ , respectively.
5. The average intensity of a hydrogen band wave event during active conditions in the afternoon sector, where the waves are most frequent, is of the order  $0.5 \text{ nT}^2$ . However, the time-averaged intensity of the hydrogen band EMIC waves during active conditions in this region is about a factor of 50 lower.
6. The average peak frequency and width of the moderate and strong hydrogen band wave events ( $B_w^2 > 0.1 \text{ nT}^2$ ) during active conditions, in the afternoon sector where the waves are most frequent, is  $0.4f_{cp}$  and  $0.05f_{cp}$ , respectively.

The data on the spectral properties and the distribution of the hydrogen band and helium band EMIC waves provided here can be used to calculate energy and pitch angle diffusion coefficients [Glauert and Horne, 2005] and used in radiation belt models [e.g., Glauert et al., 2014], to assess the role of EMIC waves in radiation belt dynamics and to improve radiation belt forecasts.

### Acknowledgments

We would like to thank Roger R. Anderson for providing the plasma frequencies used in this study. We also thank the NSSDC Omniweb for the provision of the geomagnetic activity indices used in this report. This study is part of the British Antarctic Survey Polar Science for Planet Earth Programme. The research leading to these results has received funding from the Natural Environment Research Council, the European Union Seventh Framework Programme (FP7/2007-2013) under grant agreements 262468 (SPACECAST) and 284520 (MAARBLE) and the Australian Research Council under project grant DP0222505 and linkage grant LX0882515. The data used to generate the plots in this paper are stored at the BAS Polar Data Centre and are available on request.

M. Balikhin thanks Andrei Demekhov and Richard Denton for their assistance in evaluating the paper.

### References

- Anderson, B. J., and D. C. Hamilton (1993), Electromagnetic ion cyclotron waves stimulated by modest magnetospheric compressions, *J. Geophys. Res.*, *98*, 11,369–11,382, doi:10.1029/93JA00605.
- Anderson, B. J., R. E. Erlandson, and L. J. Zanetti (1992a), A statistical study of Pc 1-2 magnetic pulsations in the equatorial magnetosphere: 1. Equatorial occurrence distributions, *J. Geophys. Res.*, *97*, 3075–3088.
- Anderson, R. R., D. A. Gurnett, and D. L. Odem (1992b), CRRES plasma wave experiment, *J. Spacecr. Rockets*, *29*, 570–573.
- Arnoldy, R. L., et al. (2005), Pc 1 waves and associated unstable distributions of magnetospheric protons observed during a solar wind pressure pulse, *J. Geophys. Res.*, *110*, A07229, doi:10.1029/2005JA011041.
- Baker, D. N. (2001), Satellite anomalies due to space storms, in *Space Storms and Space Weather Hazards*, edited by I. A. Daglis, 251 pp., Springer, New York.
- Baker, D. N., J. B. Blake, R. W. Klebesadel, and P. R. Higbie (1986), Highly relativistic electrons in the Earth's outer magnetosphere. 1. Lifetimes and temporal history 1979–1984, *J. Geophys. Res.*, *19*(A4), 4265–4276.
- Baker, D. N., J. B. Blake, L. B. Callis, J. R. Cummings, D. Hovestadt, S. Kanekal, B. Klecker, R. A. Mewaldt, and R. D. Zwickl (1994), Relativistic electron acceleration and decay time scales in the inner and outer radiation belts: SAMPEX, *Geophys. Res. Lett.*, *21*(6), 409–412, doi:10.1029/93GL03532.
- Baker, D. N., S. G. Kanekal, R. B. Horne, N. P. Meredith, and S. A. Glauert (2007), Low-altitude measurements of 2–6 MeV electron trapping lifetimes at  $L \leq L \leq 2.5$ , *Geophys. Res. Lett.*, *34*, L20110, doi:10.1029/2007GL031007.
- Blake, J. B., W. A. Kolasinski, R. W. Fillius, and E. G. Mullen (1992), Injection of electrons and protons with energies of tens of MeV into  $L < 3$  on 24 March 1991, *Geophys. Res. Lett.*, *19*(8), 821–824.
- Bossen, M., R. L. McPherron, and C. T. Russell (1976), A statistical study of Pc 1 magnetic pulsations at synchronous orbit, *J. Geophys. Res.*, *81*, 6083–6091.
- Bräysy, T., K. Mursula, and G. Markland (1998), Ion cyclotron waves during a great geomagnetic storm observed by Freja double-probe electric field instrument, *J. Geophys. Res.*, *103*, 4145–4155.

- Carson, B. R., C. J. Rodger, and M. A. Clilverd (2013), POES satellite observations of EMIC-wave driven relativistic electron precipitation during 1998–2010, *J. Geophys. Res. Space Physics*, *118*, 232–243, doi:10.1029/2012JA017998.
- Clausen, L. B. N., J. B. H. Baker, J. M. Ruohoniemi, and H. J. Singer (2011), EMIC waves observed at geosynchronous orbit during solar minimum: Statistics and excitation, *J. Geophys. Res.*, *116*, A10205, doi:10.1029/2011JA016823.
- Clilverd, M. A., C. J. Rodger, R. M. Millan, J. G. Sample, M. Kokorowski, M. P. McCarthy, T. Ulich, T. Raita, A. J. Kavanagh, and E. Spanswick (2007), Energetic particle precipitation into the middle atmosphere triggered by a coronal mass ejection, *J. Geophys. Res.*, *112*, A12206, doi:10.1029/2007JA012395.
- Cornwall, J. M., F. V. Coroniti, and R. M. Thorne (1970), Turbulent loss of ring current protons, *J. Geophys. Res.*, *75*, 4699–4709.
- Dachev, Ts. P., et al. (2013), Relativistic electron fluxes and dose rate variations observed on the international space station, *J. Atmos. Sol. Terr. Phys.*, *99*, 150–156.
- Denton, M. H., and J. E. Borovsky (2008), Superposed epoch analysis of high-speed-stream effects at geosynchronous orbit: Hot plasma, cold plasma, and the solar wind, *J. Geophys. Res.*, *113*, A07216, doi:10.1029/2007JA012998.
- Erlanson, R. E., and A. J. Ukhorskiy (2001), Observations of electromagnetic ion cyclotron waves during geomagnetic storms: Wave occurrence and pitch angle scattering, *J. Geophys. Res.*, *106*(A3), 3883–3895, doi:10.1029/2000JA000083.
- Fraser, B. J., and R. L. McPherron (1982), Pc 1-2 magnetic pulsation spectra and heavy ion effects at synchronous orbit: ATS 6 results, *J. Geophys. Res.*, *87*, 4560–4566.
- Fraser, B. J., and T. S. Nguyen (2001), Is the plasmopause a preferred source region of electromagnetic ion cyclotron waves in the magnetosphere? *J. Atmos. Sol. Terr. Phys.*, *63*, 1225–1247.
- Glauert, S. A., and R. B. Horne (2005), Calculation of pitch angle and energy diffusion coefficients with the PADIE code, *J. Geophys. Res.*, *110*, A04206, doi:10.1029/2004JA010851.
- Glauert, S. A., R. B. Horne, and N. P. Meredith (2014), Three dimensional electron radiation belt simulations using the BAS Radiation Belt Model with new diffusion models for chorus, plasmaspheric hiss and lightning generated whistlers, *J. Geophys. Res. Space Physics*, *119*, 268–289, doi:10.1002/2013JA019281.
- Horne, R. B. (2002), The contribution of wave-particle interactions to electron loss and acceleration in the Earth's radiation belts during geomagnetic storms, in *URSI Review of Radio Science 1999-2002*, edited by W. R. Stone, pp. 801–828, Wiley, New York.
- Horne, R. B., and R. M. Thorne (1994), Convective instabilities of electromagnetic ion cyclotron waves in the outer magnetosphere, *J. Geophys. Res.*, *99*, 17,259–17,273.
- Horne, R. B., and R. M. Thorne (1998), Potential waves for relativistic electron scattering and stochastic acceleration during magnetic storms, *Geophys. Res. Lett.*, *25*, 3011–3014.
- Horne, R. B., M. M. Lam, and J. C. Green (2009), Energetic electron precipitation from the outer radiation belt during geomagnetic storms, *Geophys. Res. Lett.*, *36*, L19104, doi:10.1029/2009GL040236.
- Johnson, M. H., and J. Kierein (1992), Combined Release and Radiation Effects Satellite (CRRES): Spacecraft and mission, *J. Spacecr. Rockets*, *29*, 556–563.
- Jordanova, V. K., C. J. Farrugia, R. M. Thorne, G. V. Khazanov, G. D. Reeves, and M. F. Thomsen (2001), Modeling ring current proton precipitation by electromagnetic ion cyclotron waves during the May 14–16, 1997, storm, *J. Geophys. Res.*, *106*, 7–22.
- Keika, K., K. Takahashi, A. Y. Ukhorskiy, and Y. Miyoshi (2013), Global characteristics of electromagnetic ion cyclotron waves: Occurrence rate and its storm dependence, *J. Geophys. Res. Space Physics*, *118*, 4135–4150, doi:10.1002/jgra.50385.
- Kennel, C. F., and H. E. Petschek (1966), Limit on stably trapped particle fluxes, *J. Geophys. Res.*, *71*(1), 1–28, doi:10.1029/JZ071i001p00001.
- Kozyra, J. U., T. E. Cravens, A. F. Nagy, E. G. Fonthelm, and R. S. B. Ong (1984), Effects of energetic heavy ions on electromagnetic ion cyclotron wave generation in the plasmopause region, *J. Geophys. Res.*, *89*, 2217–2233.
- Loto'aniu, T. M., B. J. Fraser, and C. L. Waters (2005), Propagation of electromagnetic ion cyclotron wave energy in the magnetosphere, *J. Geophys. Res.*, *110*, A07214, doi:10.1029/2004JA010816.
- Lyons, L. R., and R. M. Thorne (1972), Parasitic pitch angle diffusion of radiation belt particles by ion cyclotron waves, *J. Geophys. Res.*, *77*, 5608–5616.
- McCullough, J. P., J. L. Gannon, D. N. Baker, and M. Gehmeyr (2008), A statistical comparison of commonly used external magnetic field models, *Space Weather*, *6*, S10001, doi:10.1029/2008SW000391.
- Meredith, N. P., R. B. Horne, D. Summers, R. M. Thorne, R. H. A. Iles, D. Heynderickx, and R. R. Anderson (2002), Evidence for acceleration of outer zone electrons to relativistic energies by whistler mode chorus, *Ann. Geophys.*, *20*, 967–979.
- Meredith, N. P., R. M. Thorne, R. B. Horne, D. Summers, B. J. Fraser, and R. R. Anderson (2003), Statistical analysis of relativistic electron energies for cyclotron resonance with EMIC waves observed on CRRES, *J. Geophys. Res.*, *108*(A6), 1250, doi:10.1029/2002JA009700.
- Meredith, N. P., R. B. Horne, M. M. Lam, M. H. Denton, J. E. Borovsky, and J. C. Green (2011), Energetic electron precipitation during high-speed solar wind stream driven storms, *J. Geophys. Res.*, *116*, A05223, doi:10.1029/2010JA016293.
- Meredith, N. P., R. B. Horne, A. Sicard-Piet, D. Boscher, K. H. Yearby, W. Li, and R. M. Thorne (2012), Global model of lower band and upper band chorus from multiple satellite observations, *J. Geophys. Res.*, *117*, A12209, doi:10.1029/2012JA017978.
- Millan, R. M., R. P. Lin, D. M. Smith, and M. P. McCarthy (2007), Observation of relativistic electron precipitation during a rapid decrease of trapped relativistic electron flux, *Geophys. Res. Lett.*, *34*, L10101, doi:10.1029/2006GL028653.
- Miyoshi, Y., K. Sakaguchi, K. Shiokawa, D. Evans, J. Albert, M. Connors, and V. Jordanova (2008), Precipitation of radiation belt electrons by EMIC waves, observed from ground and space, *Geophys. Res. Lett.*, *35*, L23101, doi:10.1029/2008GL035727.
- Morley, S. K., S. T. Ables, M. D. Sciffer, and B. J. Fraser (2009), Multipoint observations of Pc1-2 waves in the afternoon sector, *J. Geophys. Res.*, *114*, A09205, doi:10.1029/2009JA014162.
- Olson, W. P., and K. Pfitzer (1977), Magnetospheric magnetic field modelling annual scientific report, AFOSR Contract No. F44620-75-c-0033.
- Paulikas, G. A., and J. B. Blake (1979), Effects of the solar wind on magnetospheric dynamics: Energetic electrons at synchronous orbit, in *Quantitative Modeling of Magnetospheric Processes*, *Geophys. Monogr. Ser.*, vol. 21, edited by W. P. Olsen, 180 pp., AGU, Washington, D. C.
- Pickett, J. S., et al. (2010), Cluster observations of EMIC triggered emissions in association with Pc1 waves near Earth's plasmopause, *Geophys. Res. Lett.*, *37*, L09104, doi:10.1029/2010GL042648.
- Reeves, G. D., K. L. McAdams, R. H. W. Friedel, and T. P. O'Brien (2003), Acceleration and loss of relativistic electrons during geomagnetic storms, *Geophys. Res. Lett.*, *30*(10), 1529, doi:10.1029/2002GL016513.
- Rodger, C. J., T. Raita, M. A. Clilverd, A. Seppälä, S. Dietrich, N. R. Thomson, and T. Ulich (2008), Observations of relativistic electron precipitation from the radiation belts driven by EMIC waves, *Geophys. Res. Lett.*, *35*, L16106, doi:10.1029/2008GL034804.
- Roederer, J. G. (1970), *Dynamics of Geomagnetically Trapped Radiation*, Springer, New York.

- Roux, A., S. Perraut, J. L. Rauch, C. de Villedary, G. Kremser, A. Korth, and D. T. Young (1982), Wave-particle interactions near  $\Omega H^+$  observed on board GEOS 1 and 2. Generation of ion cyclotron waves and heating of  $He^+$  ions, *J. Geophys. Res.*, *87*, 8174–8190.
- Sakaguchi, K., K. Shiokawa, A. Ieda, Y. Miyoshi, Y. Otsuka, T. Ogawa, M. Connors, E. F. Donovan, and F. J. Rich (2007), Simultaneous ground and satellite observations of an isolated proton arc at subauroral latitudes, *J. Geophys. Res.*, *112*, A04202, doi:10.1029/2006JA012135.
- Singer, H. J., W. P. Sullivan, P. Anderson, F. Mozer, P. Harvey, J. Wygant, and W. McNeil (1992), Fluxgate magnetometer instrument on the CRRES, *J. Spacecr. Rockets*, *29*, 599–601.
- Summers, D., and R. M. Thorne (2003), Relativistic electron pitch-angle scattering by electromagnetic ion cyclotron waves during geomagnetic storms, *J. Geophys. Res.*, *108*(A4), 1143, doi:10.1029/2002JA009489.
- Summers, D., R. M. Thorne, and F. Xiaio (1998), Relativistic theory of wave-particle resonant diffusion with application to electron acceleration in the magnetosphere, *J. Geophys. Res.*, *103*, 20,487–20,500.
- Thorne, R. M. (1974), A possible cause of dayside relativistic electron precipitation events, *J. Atmos. Terr. Phys.*, *36*, 635–645.
- Thorne, R. M. (2010), Radiation belt dynamics: The importance of wave-particle interactions, *Geophys. Res. Lett.*, *37*, L22107, doi:10.1029/2010GL044990.
- Thorne, R. M., and L. J. Andreoli (1980), Mechanisms for intense relativistic electron precipitation, in *Exploration of the Polar Upper Atmosphere*, edited by C. S. Deehr and J. A. Holtet, p. 381, D. Reidel Pub. Co., Hingham, Mass.
- Thorne, R. M., and C. F. Kennel (1971), Relativistic electron precipitation during magnetic storm main phase, *J. Geophys. Res.*, *76*, 4446–4453.
- Turner, D. L., Y. Y. Shprits, M. Hartinger, and V. Angelopoulos (2012), Explaining sudden losses of outer radiation belt electrons during geomagnetic storms, *Nat. Phys.*, *8*, 208–212, doi:10.1038/nphys21851.
- Usanova, M. E., I. R. Mann, I. J. Rae, Z. C. Kale, V. Angelopoulos, J. W. Bonnell, K.-H. Glassmeier, H. U. Auster, and H. J. Singer (2008), Multi-point observations of magnetospheric compression-related EMIC Pc1 waves by THEMIS and CARISMA, *Geophys. Res. Lett.*, *35*, L17S25, doi:10.1029/2008GL034458.
- Usanova, M. E., I. R. Mann, J. Bortnik, L. Shao, and V. Angelopoulos (2012), THEMIS observations of electromagnetic ion cyclotron wave occurrence: Dependence on AE, SYMH, and solar wind dynamic pressure, *J. Geophys. Res.*, *117*, A10218, doi:10.1029/2012JA018049.
- Van Allen, J. A., and L. A. Frank (1959), Radiation around the Earth to a radial distance of 107,400 km, *Nature*, *183*, 430–434.
- Wrenn, G. L. (1995), Conclusive evidence for internal dielectric charging anomalies on geosynchronous communications spacecraft, *J. Spacecr. Rockets*, *32*, 514–520.
- Wrenn, G. L., D. J. Rodgers, and K. A. Ryden (2002), A solar cycle of spacecraft anomalies due to internal charging, *Ann. Geophys.*, *20*, 953–956.
- Yahnin, A. G., T. A. Yahnina, and H. U. Frey (2007), Subauroral proton spots visualize the Pc1 source, *J. Geophys. Res.*, *112*, A10223, doi:10.1029/2007JA012501.
- Yahnina, T. A., A. G. Yahnin, J. Kangas, J. Manninen, D. S. Evans, A. G. Demekov, V. Yu. Trakhtengerts, M. F. Thomsen, G. D. Reeves, and B. B. Gvozdevsky (2003), Energetic particle counterparts for geomagnetic pulsations of Pc1 and IPDP types, *Ann. Geophys.*, *21*, 2281–2292.
- Yahnina, T. A., H. U. Frey, T. Bisinger, and A. G. Yahnin (2008), Evidence for subauroral proton flashes on the dayside as the result of the ion cyclotron interaction, *J. Geophys. Res.*, *113*, A07209, doi:10.1029/2008JA013099.
- Yuan, Z., X. Deng, X. Lin, Y. Pang, M. Zhou, P. M. E. Décréau, J. G. Trotignon, E. Lucek, H. U. Frey, and J. Wang (2010), Link between EMIC waves in a plasmaspheric plume and a detached sub-auroral proton arc with observations of Cluster and IMAGE satellites, *Geophys. Res. Lett.*, *37*, L07108, doi:10.1029/2010GL042711.